Int. J. Heat Mass Transfer. Vol. 29, No. 11, pp. 1695–1709, 1986
Printed in Great Britain

0017–9310/86 $3.00 + 0.00
Pergamon Journals Ltd.

Experimental and numerical investigation of double-diffusive convection induced by a discrete heat source

T. L. BERGMAN† and A. UNGAN‡

† Department of Mechanical Engineering, University of Texas at Austin, Austin, TX 78712, U.S.A.
‡ School of Engineering and Technology at Indianapolis, Purdue University, Indianapolis, IN 46223, U.S.A.

(*Received* 13 *December* 1985 *and in final form* 7 *March* 1986)

Abstract—Various engineering systems, such as those associated with crystal growth techniques or solar ponds, may be characterized by double-diffusive behavior induced by discrete heat sources. Due to the relevance of such systems, the objective of this study is to investigate double-diffusive convection induced by bottom heating with a finite, heated strip placed beneath a salt-stratified layer. Attention is focused on the formation and growth of convecting regions in the salt-stratified fluid. Experimental and numerical results reveal that development of convective conditions is characterized by an interaction between Rayleigh–Bénard-type convection and longitudinal convective rolls formed by horizontal temperature gradients. Secondary flow is visualized and predicted to occur above the bottom convection cell. For relatively unstable combinations of the salt stratification and applied heat flux, a complicated interaction between chaotic, double-diffusive convection and a three-dimensional, gravity wave distribution are observed.

INTRODUCTION

RECENT interest in engineering and geophysical systems characterized by double-diffusive convection has stimulated experimental and analytical investigation of this phenomena. Due to the importance of double-diffusion in the microstructure of the upper ocean [1], mantle convection [2], the salt-gradient solar pond [3] and crystal growth [4], considerable attention has been given to species-stratified fluid layers which are destabilized by a uniform bottom heat flux [5, 6] or a uniform warm bottom temperature [7, 8].

Other engineering systems, however, may be characterized by double-diffusive behavior driven by thermal instabilities induced by discrete heat sources. For example, some crystal growth techniques involve double-diffusive phenomena associated with simultaneous heat transfer and solute rejection occurring at the interface separating a growing crystal from the parent melt [9, 10]. Possible non-uniformities in the bottom heat flux, or release of buoyant elements due to heat exchanger leakage, in salt-gradient solar ponds [11], and development of speed measurement devices utilizing heated thermistor beads for use in salt-stratified fluid layers [12], also warrant the investigation of double-diffusive convection induced by discrete heat sources.

Despite the relevance of double-diffusive convection driven by finite heat sources, little work has been done in this area. Experimental studies have been limited to the consideration of heated cylinders [13, 14] and point heated sources [15] positioned in a salt-stratified fluid layer. Numerical simulation of such systems has, apparently, not been attempted.

Due to the importance of double-diffusive convection of this nature and the paucity of information concerning these systems, the objective of this study is to investigate such systems with experimental and analytical techniques. The discrete heat source, in the current study, is a heated strip placed beneath a salt-stratified fluid layer. Attention is focused on the formation and growth of convecting regions in the salt-stratified fluid.

EXPERIMENTAL METHODS

Experiments were performed in an acrylic test cell of square base (305 × 305 mm) and 200 mm height. The test cell was equipped with a heated strip (305 × 102 mm) which extended across its base. With this arrangement, the bottom surface of the test cell was divided into three segments of equal area with the heated section separating two adiabatic sections.

A 25-mm acrylic sheet served as the bottom of the test cell. The heated section was installed in a milled groove on the upper face of the acrylic sheet so that the top of the heated section was flush with the upper surface of the acrylic. The test apparatus was designed to provide nearly uniform heating above the center section while minimizing lateral heat conduction to the acrylic. The heater was constructed in a sandwich configuration and consisted of (from top to bottom): (i) a 3.2-mm copper plate; (ii) an electric resistance patch heater (main heater); (iii) a 305 × 98 × 19 mm insulating styrofoam sheet; and (iv) an electric resistance (guard) heater.

High thermal conductivity grease was applied between the copper plate and the main heater to minimize thermal contact resistance. Thermistors

NOMENCLATURE

c	specific heat
D	binary diffusion coefficient
g	gravitational acceleration
H	height of the salt-stratified layer
H^*	height of the computational domain
k	thermal conductivity
L	half-width of the enclosure
L_b	half-width of the heated strip
m_s	salt mass fraction
P	pressure
P_0	hydrostatic pressure
q_b	applied bottom heat flux
Ra_s^*	solutal Rayleigh number, $g\beta_s(\partial m_s/\partial z)L^4/\alpha\nu$
Ra_T^*	modified thermal Rayleigh number, $g\beta_T q_b L^4/k\alpha\nu$
T	temperature
t	time
u, w	x and z velocity components
X	ratio of modified thermal Rayleigh number to solutal Raleigh number, $\beta_T q_b/k\beta_s(\partial m_s/\partial z)$
x, z	horizontal and vertical Cartesian coordinates.

Greek symbols

α	thermal diffusivity, $k/(\rho c)$
β_s	solutal expansion coefficient, $\rho^{-1}\partial\rho/\partial m_s\|_T$
β_T	thermal expansion coefficient, $\rho^{-1}\partial\rho/\partial T\|_{m_s}$
ρ	mass density
ν	kinematic viscosity.

Subscripts

0	ambient or reference conditions.

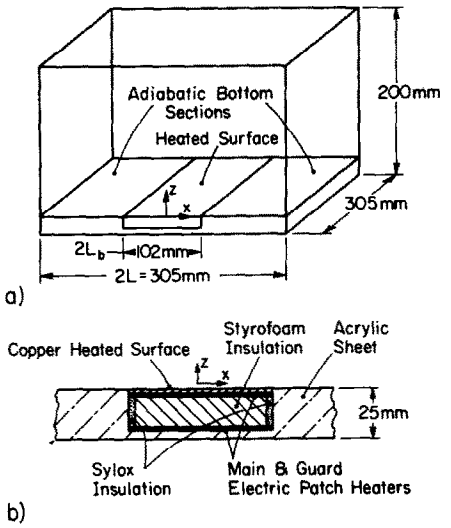

FIG. 1. (a) Schematic of the test cell; (b) cross-sectional view of the heater assembly.

were installed above and below the styrofoam sheet. Their output was monitored by an electronic control circuit which adjusted the power to the guard heater, so as to maintain temperature differences across the styrofoam to $\pm 0.10°C$. The 2-mm gaps on either side of the styrofoam were filled with Sylox [16] insulation to minimize lateral heat transfer to the acrylic base plate. The heater complex was anchored in the acrylic sheet and waterproofed with silicon.

A schematic of the test cell and a cross-sectional view of the heater assembly is shown in Fig. 1.

The experiments were performed with a 180-mm-deep, salt-stratified water layer. The top of the test cell was covered prior to application of bottom heating to minimize evaporative heat loss during the waiting period associated with establishment of the initial, nearly linear, salt distribution. The walls of the test cell were insulated with 25-mm styrofoam sheets. Details of the procedures used to construct and evaluate the initial salinity profile, and further information regarding the test cell are available elsewhere [17].

Vertical temperature distributions were measured at two locations within the fluid with arrays of copper–constantan thermocouples. The thermocouples were housed in rakes and were located at 10-mm vertical intervals (as well as at elevations of 2 and 5 mm) on the rake which was positioned in the center of the test cell and at 6.4-mm intervals on the rake which was placed in the center of one of the acrylic (adiabatic) bottom sections.

Visualization of the convective flow was obtained by shadowgraphic techniques and fluorescein dye injection. Fluorescein disodium salt was mixed with salt water which was extracted from the bottom of the fluid layer with a syringe and hypodermic prior to bottom heating. After mixing, the dyed solution was cooled to approximately 5°C and was carefully reinjected onto the bottom surface with the hypodermic. Since the injected dye was relatively cool, its initial motion was to spread evenly over the bottom surface. The dye was allowed to reach thermal equilibrium with the surrounding fluid and, as such, was nearly neutrally buoyant at the initiation of the experiment. With this visualization scheme, the fluorescing dye can be used to mark convective flow initiated at the bottom heated strip.

The dye was illuminated with a vertical sheet of light (approximately 1 mm thick) produced by expanding a

50-mW argon laser beam with a cylindrical lens. The light sheet was bounced off a mirror positioned above the test cell, requiring removal of the top cover during flow visualization. The dye was photographed with a 35-mm camera. The shadowgraph was visually monitored and was used primarily to detect the development of multiple layers above the bottom convecting region.

MATHEMATICAL MODEL

The governing equations which describe system behavior are conservation of mass, momentum, energy and species. Since small species and temperature differences exist within the system, the thermophysical properties of the fluid are assumed to be constant, and the Boussinesq approximation is invoked [18]. The system is assumed to be two-dimensional and the Dufour and Soret effects are ignored. As such, the governing equations are

$$\frac{\partial u}{\partial x}+\frac{\partial w}{\partial z}=0 \tag{1}$$

$$\frac{\partial w}{\partial t}+u\frac{\partial w}{\partial x}+w\frac{\partial w}{\partial z}=-\frac{1}{\rho_0}\frac{\partial p}{\partial z}-g[\beta_T(T-T_0)-\beta_s(m_s-m_{s0})]+\nu\frac{\partial^2 w}{\partial x}+\nu\frac{\partial^2 w}{\partial z} \tag{2}$$

$$\frac{\partial u}{\partial t}+u\frac{\partial u}{\partial x}+w\frac{\partial u}{\partial z}=-\frac{1}{\rho_0}\frac{\partial p}{\partial x}+\nu\frac{\partial^2 u}{\partial x^2}+\nu\frac{\partial^2 u}{\partial z^2} \tag{3}$$

$$\frac{\partial T}{\partial t}+u\frac{\partial T}{\partial x}+w\frac{\partial T}{\partial z}=\alpha\frac{\partial^2 T}{\partial x^2}+\alpha\frac{\partial^2 T}{\partial z^2} \tag{4}$$

$$\frac{\partial m_s}{\partial t}+u\frac{\partial m_s}{\partial x}+w\frac{\partial m_s}{\partial z}=D\frac{\partial^2 m_s}{\partial x^2}+D\frac{\partial^2 m_s}{\partial z^2}. \tag{5}$$

Since the system is symmetric about $x = 0$, it is necessary to consider only half of the rectangular cross-section of the test cell in the model. Accordingly, the boundaries of the computational domain are, in general, formed by a rectangle of height, H, and length, L. The fluid is surrounded by adiabatic, no-slip, impermeable walls at the side and bottom, except at the heated strip where an appropriate heat flux is imposed. Although there is a free surface in the experimental phase of the study, heat losses from the top of the computational domain are assumed to be negligible. This assumption is valid until thermal effects penetrate to the free surface. Accordingly, equations (1)–(5) are subject to the following boundary conditions

$$u=0,\quad \frac{\partial w}{\partial x}=\frac{\partial T}{\partial x}=\frac{\partial m_s}{\partial x}=0 \quad \text{at } x=0 \tag{6a}$$

$$u=w=0,\quad \frac{\partial T}{\partial x}=\frac{\partial m_s}{\partial x}=0 \quad \text{at } x=L \tag{6b}$$

Table 1. Experimental conditions

Experiment	q_b (W m^{-2})	$(\partial m_s/\partial z)_i$ (% m^{-1})	X
1	300	15.0	1.0
2	300	5.0	3.0
3	1500	25.0	3.0
4	600	2.50	12.0
5	1200	1.25	48.0

$$u=w=0,\quad q_b=-k\frac{\partial T}{\partial z},\quad \frac{\partial m_s}{\partial z}=0 \quad \text{at } z=0,\quad 0<x<L_b \tag{6c}$$

$$u=w=0,\quad \frac{\partial T}{\partial z}=\frac{\partial m_s}{\partial z}=0 \quad \text{at } z=0,\quad L_b<x<L \tag{6d}$$

$$w=0,\quad \frac{\partial u}{\partial z}=\frac{\partial T}{\partial z}=\frac{\partial m_s}{\partial z}=0 \quad \text{at } z=H. \tag{6e}$$

The system is assumed to be initially quiescent and isothermal at an ambient temperature of $T = T_0$. The initial salinity profile was determined from the appropriate experiment and was used as an initial condition in the numerical prediction. The thermophysical properties were evaluated at the mean salinity and T_0, according to the relations of ref. [19].

The governing equations were discretized using the control volume approach of Patankar [20] and solved with a fully implicit scheme. The power law formulation [20] was employed to determine the combined (convective and diffusive) fluxes across the boundaries of each control volume. The discretized equations were solved iteratively by the line-by-line procedure of the tri-diagonal matrix algorithm. The dynamic component of the pressure was calculated by means of the SIMPLER algorithm [20, 21].

Within each time step, the convergence criterion was such that the maximum relative change between consecutive iterations is less than 10^{-4} and that the residual sources of mass, energy, species and momentum are less than 10^{-3}.

EXPERIMENTAL RESULTS

Five experiments were performed with various applied heat fluxes, q_b, and stabilizing salinity gradients, $\partial m_s/\partial z$. The relative influence of the destabilizing temperature and stabilizing salinity gradients for a particular experiment is described by the ratio of the modified thermal to solutal Rayleigh numbers [22]

$$X\equiv\frac{Ra_T^*}{Ra_s^*}=\frac{\beta_T q_b}{k\beta_s(\partial m_s/\partial z)}. \tag{7}$$

Values of q_b, $\partial m_s/\partial z$ and X are shown in Table 1 for the five experiments.

Typical flow visualization results are shown in Figs. 2–4 for experiments 2, 4 and 5, respectively. The bottom of the test cell is delineated by a bright, horizontal

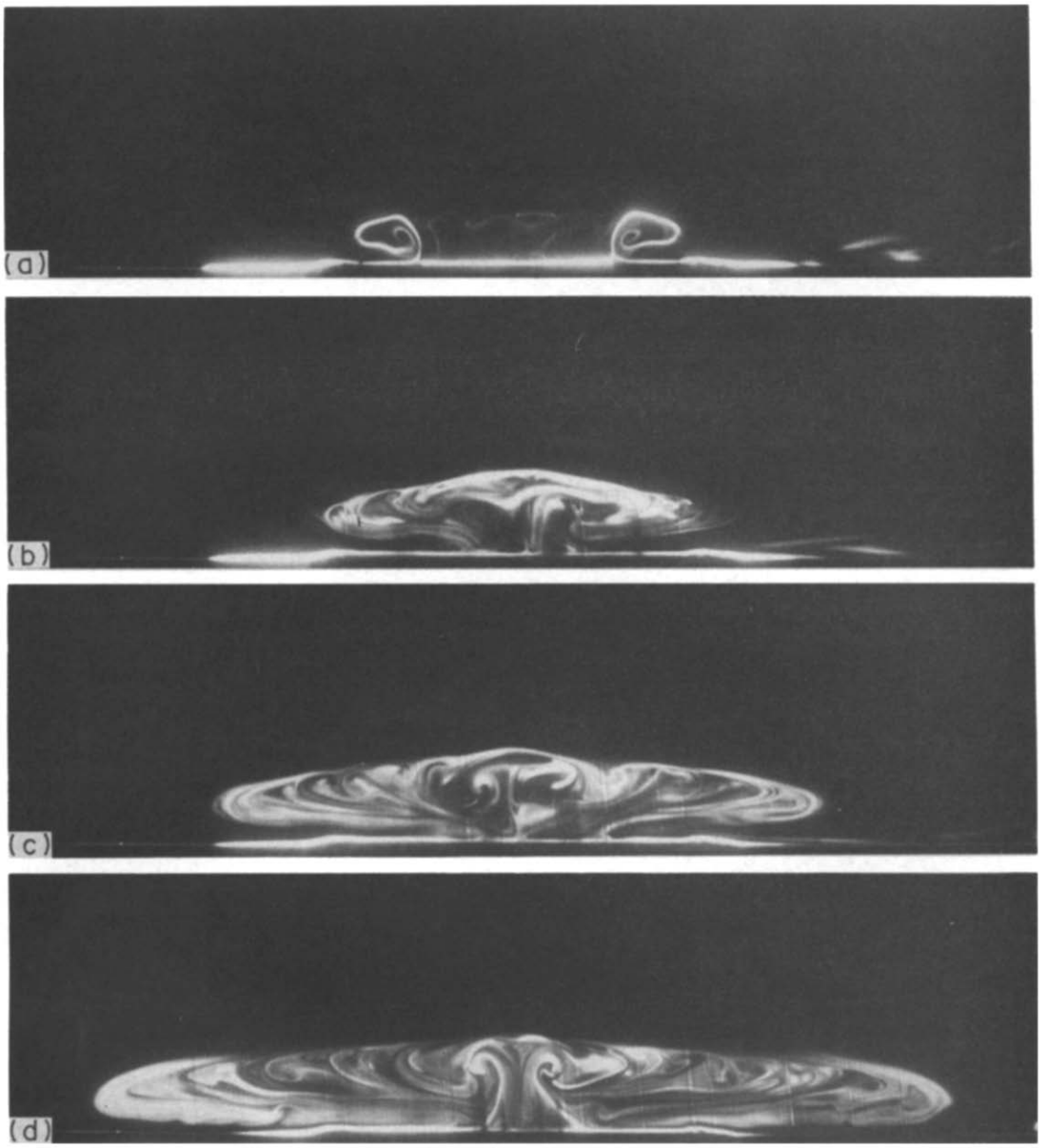

FIG. 2. Dye visualization of experiment 2: (a) $t = 150$ s; (b) $t = 270$ s; (c) $t = 390$ s; (d) $t = 630$ s.

line of fluorescein in each of the figures. The horizontal span of the photographs corresponds to the width of the test cell (305 mm).

As seen in the figures, convective motion is induced by bottom heating and the vertical propagation of mixed conditions is suppressed by the salt stratification. The upward penetration of convective conditions increases as X increases (Figs. 2–4).

In experiment 2 (Fig. 2), thermal instabilities promote convection which begins at the boundaries separating the heated strip and the adiabatic sections of the bottom surface. A non-uniform, horizontal distribution of the vertical, thermally-induced buoyancy forces drives rotational fluid motion which is evidenced by the spiralling dye streaks (Fig. 2a, $t = 150$ s). A series of weak, randomly-located dye plumes are also evident above the heated surface between the dye spirals. The relative absence of dye in the intermediate plumes suggests that they are characterized by small convective velocities.

Observation of the initial stages of the convective process showed that the horizontal span of the counter-rotating cells associated with the dyed spirals increases. The dye spirals scrolled toward each other while consuming the intermediate, weaker convection cells. The two main convection cells eventually merged at the center line of the heated strip and coalesced to form a larger, 'squashed mushroom' convective region shown in Fig. 2b ($t = 270$ s).

Warm fluid ascends from the center of the heated strip and impinges upon the overlying salt-stratified fluid. The ascending stream bifurcates and establishes

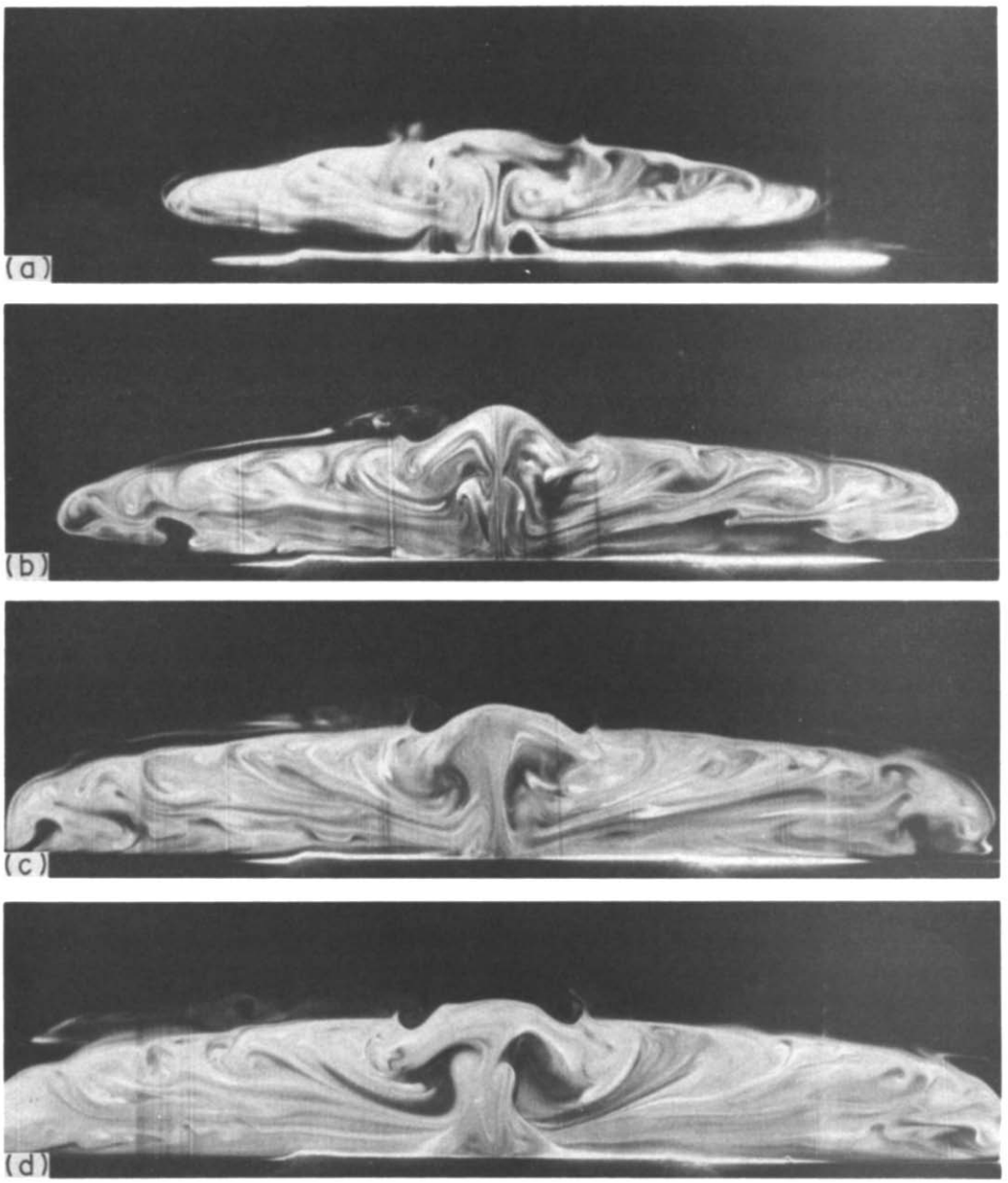

FIG. 3. Dye visualization of experiment 4: (a) $t = 210$ s; (b) $t = 360$ s; (c) $t = 510$ s; (d) $t = 780$ s.

a symmetric, horizontally propagating, convecting region similar in appearance to those reported when a salt-stratified fluid is heated from the side [23, 24]. The warm, ascending fluid is replenished with undyed fluid which is sucked into the center of the heated strip from above the adiabatic bottom sections.

As the experiment continues (Figs. 2c, d; $t = 390$, 630 s) the convecting region remains nearly constant in height while the dyed fluid spreads laterally and eventually contacts the test cell side walls. As seen in Fig. 2d, the heated fluid takes on the appearance of a small, mushroom-shaped thermal rising from the center of the heated strip. The rising fluid is subsequently cooled at the interface separating the convecting region from the undyed overlying region and descends at various locations, as evidenced by the wisps of falling fluorescein dye. Undyed fluid replenishes the ascending thermal throughout the heating process. Shadowgraph visualization indicated the absence of discernible convection above the dyed fluid region of Fig. 2.

The behavior of experiments 1 and 3, characterized by smaller and the same values of X, respectively, was qualitatively similar to that of experiment 2. But, as X is increased (experiment 4, Fig. 3), variations in system behavior are noted.

The spiral dye streaks associated with the initial stages of convection in experiment 2 are still evident, but the plumes originating above the heated strip are more energetic, and merging of the dye spirals was not observed (Fig. 3a; $t = 210$ s).

Although the interface separating the convecting

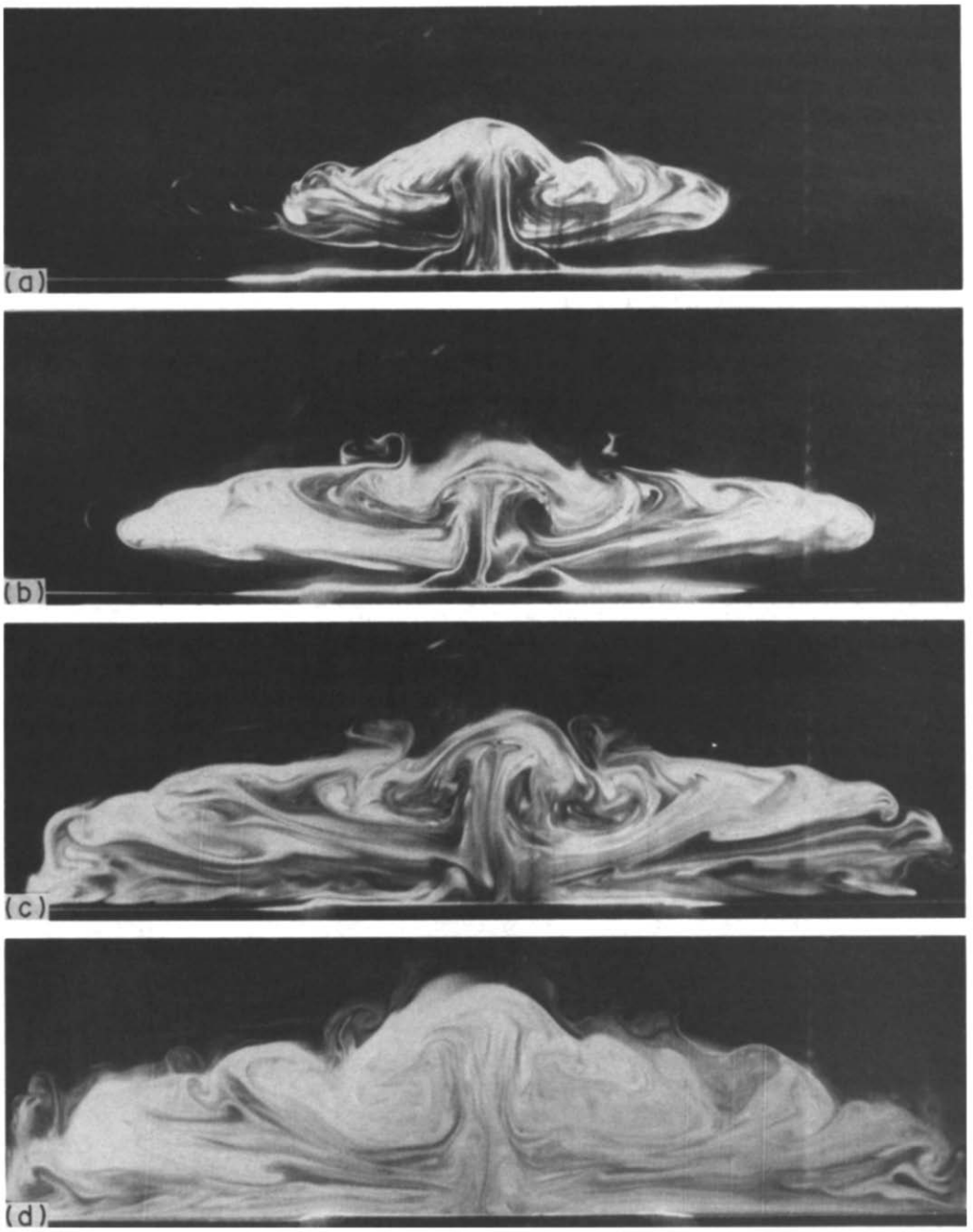

FIG. 4. Dye visualization of experiment 5: (a) $t = 120$ s; (b) $t = 180$ s; (c) $t = 360$ s; (d) $t = 750$ s.

layer from the undyed fluid was smooth for experiments 1–3, the interface was characterized by local curvature in experiment 4 (Fig. 3b; $t = 360$ s). This curvature is especially pronounced on either side of the cap of the two-dimensional thermal plume ascending from the heated strip.

Multiple convection layers were observed above the main convecting layer. Two secondary layers, in the form of longitudinal rolls, rested and rotated in the troughs on either side of the central thermal plume. These secondary rolls are indicated by the faint dye streaks evident in Figs. 3c ($t = 510$ s) and 3d ($t = 780$ s). The streaks indicate that the direction of rotation is such that the top of the roll moves toward the center of the test cell. Hence, it may be concluded that the rotational motion of the secondary rolls is induced by shear forces established at the interface resulting from the bifurcation of the thermal plume. The development of secondary convecting layers above main convecting regions has often been observed in salt-stratified fluid layers heated uniformly from below [5] and has been attributed to thermal instabilities resulting from upward heat transfer from the warm, bottom layer. The results of Fig. 3 show that shear forces may also induce secondary convective motion above the bottom convecting

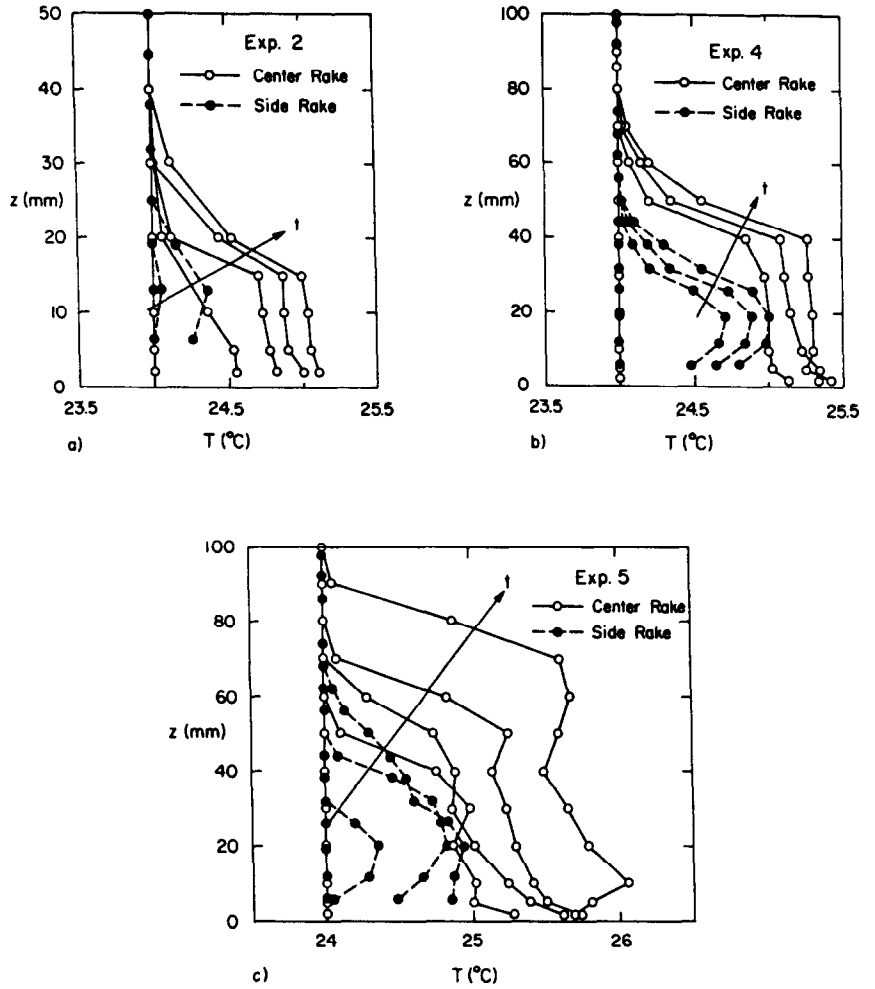

FIG. 5. Measured temperature profiles for (a) experiment 2: $t = 0$, 150, 270, 390 and 630 s; (b) experiment 4: $t = 0$, 360, 510 and 780 s; (c) experiment 5: $t = 0$, 120, 180, 360 and 750 s.

region. (The dye located above the left side of the main convecting layer is an artifact of the initial injection process. The movement of this artifact suggests that the overlying salt-stratified fluid is not stagnant, but is slowly moved by shear forces generated at the interface separating the dyed and undyed fluid.)

Tertiary convective layers are evident in Fig. 3d in the triangular regions between the bottom convective layer and the test cell side walls. These layers are indicated by the dyed horizontal fingers which extend outward from the bottom convecting layer to the test cell wall. The tertiary cells are apparently driven by side wall heat losses since shear forces in the bottom convecting layer would induce rotation in the opposite direction.

Shadowgraph visualization of the system indicated that the secondary and tertiary convection cells are present, but are characterized by very small convective velocities.

Flow visualization of the least stable experiment (experiment 5; $X = 48$) is presented in Fig. 4. A relatively strong thermal plume is induced by bottom heating and penetrates the overlying salt-stratified fluid (Fig. 4a; $t = 120$ s). The merging roll structure of Fig. 2 was not observed.

Secondary motion is evident above the highly contorted interface separating the dyed fluid from the overlying salt-stratified region (Fig. 4b; $t = 180$ s). The main convecting layer expands horizontally (Fig. 4c; $t = 360$ s) and eventually contacts the test cell side walls.

The behavior, which is shown in Fig. 4, is similar to the interaction of a thermal plume with a thermally stratified fluid region [25], except that large multiple layers were not observed above the bottom convecting region. The convective layer of experiment 5 oscillated in the vertical direction, suggesting the presence of gravity waves in the overlying salt-stratified fluid. Lateral flapping of the thermal plume was also noted. As such, very complicated system behavior, including the interaction of double-diffusive, turbulent convection with an oscillating, three-dimensional, gravity wave distribution, occurs for large X.

Measured temperature profiles are shown in Fig. 5

for experiments 2, 4 and 5. Open data symbols and solid lines represent temperatures above the center of the heated strip while closed symbols and broken lines correspond to temperatures above the middle of the adiabatic section.

Warming temperatures are associated with the expanding convection layers. As the convecting layer propagates laterally, warm fluid travels horizontally and eventually contacts the side thermocouple rake above the adiabatic section. At this location, warm fluid is concentrated in the upper half of the convecting layer, while cooler temperatures exist in the lower portion of the convective layer. This thermally-stratified temperature distribution is associated with replenishment of the thermal plume with cool, ambient fluid.

The results of Fig. 5 suggest that convective conditions become more disorganized as X increases. For example, the temperature profiles of Fig. 5a are free of inflection points, except, of course, for the large inflection associated with thermally stratified conditions above the adiabatic bottom section. As q_b and X are increased, local temperature profile inflections become evident (experiment 4; Fig. 5b) and are sometimes large (experiment 5; Fig. 5c). These results are expected since large temperature fluctuations should accompany the gravity waves which developed in experiment 5.

NUMERICAL PREDICTIONS

The flow visualization results of Figs. 2–4 are useful in describing system behavior. However, the visualization technique is limited in its ability to clarify certain features. For example, all convective fluid motion is not described by the dye visualization. Ambient fluid, which replenishes the ascending thermal plume in Figs. 2 and 3, is undyed. The dye artifact of Fig. 3 shows that the overlying, undyed, salt-stratified fluid is also in motion. Some details of the onset of convection were visually observed, but not photographically recorded. Information concerning the salinity and density distributions is unavailable. As such, it is desirable to investigate system behavior with the mathematical model which was previously described.

In the numerical simulations, attention is focused on events associated with the onset of convection at the bottom of the test cell. After several preliminary simulations, it was concluded that discretization of the entire height of the experimental domain is computationally wasteful (for experiments with small X) since neither thermal or discernible convective effects propagate to the upper portions of the salt-stratified fluid during the initial stages of an experiment. As such, a computational domain with a height of 60 mm and a non-uniformly distributed 64×29 grid was sufficient to convey the features of convective development within the system for experiments 1–3. Preliminary simulations also indicated that a time increment of 2 s leads to satisfactory simulation. However, due to the shrinkage of the computational domain, it was necessary to modify the boundary condition specified by equation (6e) and the following procedure, originally employed in ref. [26], was found to be appropriate for the present study. At $z = H^* < H$, the dynamic pressure was equated to the experimental hydrostatic pressure and vertical derivatives of w were set to zero. Ambient temperature and the initial salt mass fraction associated with $z = H^*$ are specified at locations of inflow from above $z = H^*$. At locations of outflow from the domain, the vertical derivative of T and m_s are set to zero and $\partial m_s/\partial z$, respectively. If the inflow or outflow velocities are in the order of 1 μm s^{-1}, the errors associated with the modification of equation (6e) were found to be negligible.

In the experiments characterized by large X (experiment 4), the full height of the test fluid was discretized with a 64×48 grid. The boundary conditions of equation (6) were employed, and the time increment was decreased to 0.5 s.

The predicted behavior of experiment 2 is shown in Figs. 6 and 7. Predicted streamlines and isotherms are presented in Fig. 6 while salinity and density distributions are depicted in Fig. 7. The heated section is represented by the thin rectangle beneath each figure while the centerline of the system is shown as a vertical line.

As evident in Fig. 6a, convection is predicted to initiate at the edge of the heated section. The rotational motion, indicated by the streamlines, is induced by the corresponding non-uniform destabilizing temperature distribution.

Rayleigh–Bénard-type cells appear above the plate at $t = 30$ s and at $t = 60$ s (Fig. 6b), a series of these cells spans the heated section. The large convection cell, which initially formed at the heated section's edge, has grown and has begun to propagate toward the centerline. A very weak recirculation is evident in the bottom portion of the calculation domain. Temperature profiles also indicate the existence of the two-dimensional cellular structure above the heated surface while warm temperatures are carried away from the heated section by the edge roll cell.

As the simulation continues (Fig. 6c; $t = 80$ s) the small cellular structure above the heated surface is consumed by the larger edge cell and the corresponding temperature distribution becomes less organized. A very weak recirculation is predicted to occur in the overlying salt-stratified fluid and may be induced by shear stresses due to convection in the main cell.

Merging of the edge cells is predicted to occur at $t = 130$ s. At a later time (Fig. 6d; $t = 350$ s), a single thermal plume rises from the center of the heated section and is replenished from the ambient fluid. Thermal effects begin to diffuse upward into the salt-stratified fluid as shown by the difference in elevation of the uppermost streamlines and isotherms. The lower portion of the convecting region is predicted to

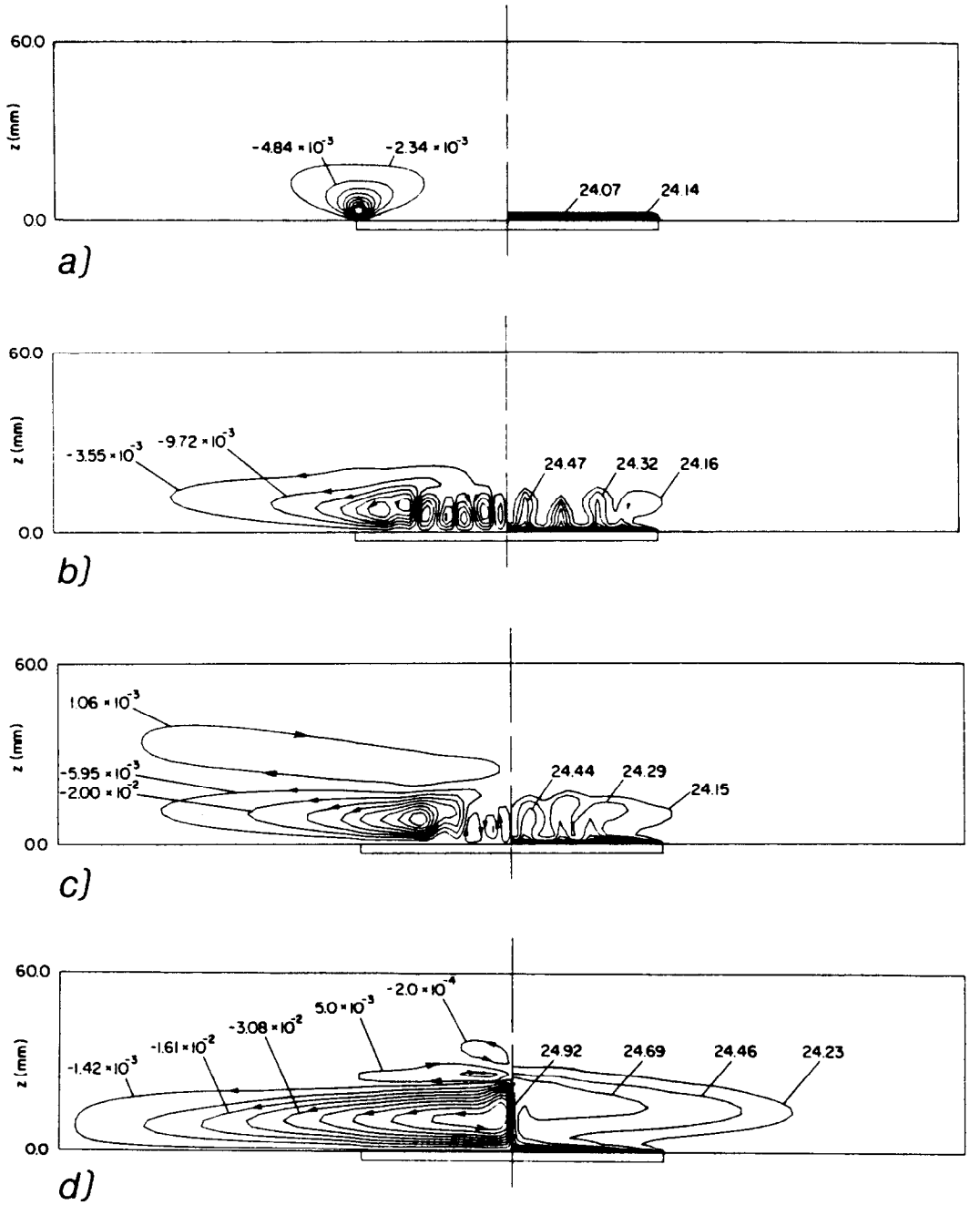

FIG. 6. Predicted streamlines (left) and isotherms (right) for experiment 2: (a) $t = 10$ s; (b) $t = 60$ s; (c) $t = 80$ s; and (d) $t = 350$ s. Streamline and temperature values are s^{-1} and °C, respectively.

be thermally stratified above the adiabatic surface. Cool, ambient fluid is warmed as it is advected across the heated surface into the center of the calculation domain.

As evident in Fig. 6c, a weak counter-rotating circulation is predicted to occur above the interface. As the simulation continues, this secondary roll cell moves toward the symmetry plane, and at $t = 350$ s (Fig. 6d) a third roll cell develops. The additional roll cells are believed to be induced by shear stresses in the horizontal direction [25]. A similar 'Christmas tree' structure has been previously observed [15] in experiments which considered a point heat source placed in a salt-stratified fluid, where the small size of the point heat source is capable of creating large horizontal temperature (or density) gradients which induce co-rotating secondary circulation.

Predicted salinity and density distributions are shown in Fig. 7 and provide details of these experimentally-unavailable quantities. The system is

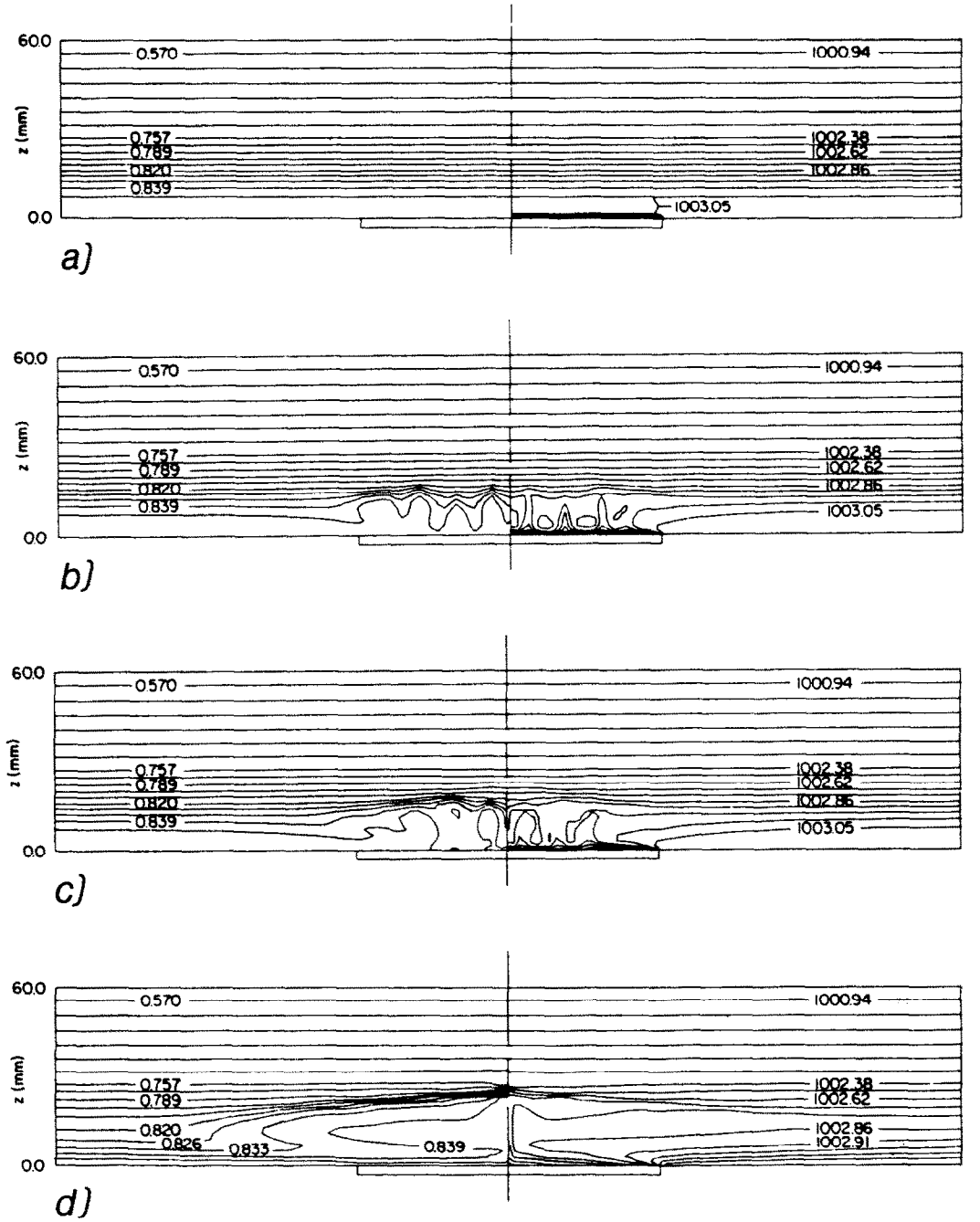

FIG. 7. Predicted salinity (left) and density (right) distributions for experiment 2: (a) $t = 10$ s; (b) $t = 60$ s; (c) $t = 80$ s; (d) $t = 350$ s. Salinity and density values are percent and kg m^{-3}, respectively.

initially salt-stratified (Fig. 7a; $t = 10$ s) with a nearly linear salinity distribution except near the impermeable bottom surface. Large unstable density gradients develop above the heated surface which induce rotation of the edge convection cell.

As the simulation continues (Fig. 7b; $t = 60$ s) the Rayleigh–Bénard cells redistribute salinities above the heated surface. As the main roll cells expand (Fig. 7c; $t = 80$ s), the salinity within the mixed layer becomes nearly uniform. Large salinity and, hence, stabilizing density gradients develop at the interface separating the convecting fluid from the salt-stratified fluid and inhibit further upward propagation of convective conditions. Finally, simulations for later times (Fig. 7d; $t = 350$ s), show that the rising thermal plume is replenished by salty ambient fluid which is also thermally stratified (Fig. 6d).

Several additional features of Figs. 6 and 7 should

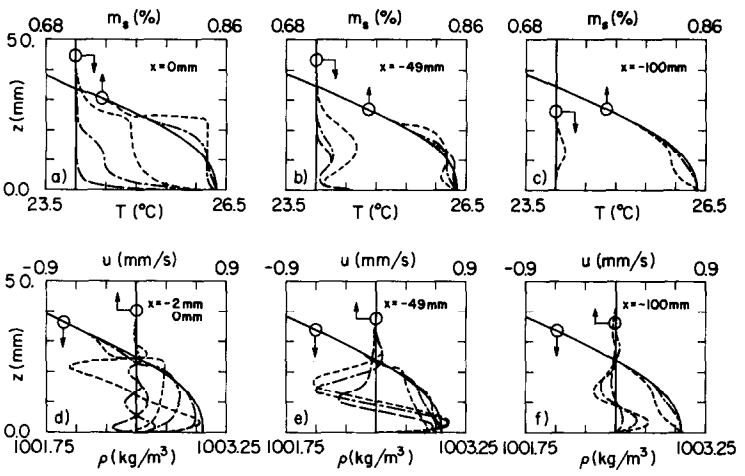

FIG. 8. Predicted vertical temperature, salinity, horizontal velocity, and density distributions above the center of the heated section (left, velocities are at $x = 2$ mm), midway above the adiabatic section (right), and at the edge of the heated strip (center). The predictions correspond to $t = 0$ s ——; $t = 60$ s — — —; $t = 130$ s — — — —; $t = 350$ s — — —, for experiment 2.

be noted. Numerical simulations included in Figs. 6 and 7 reveal similar behavior as the experimental results of Fig. 2. Unfortunately, the experimental results lag the numerical predictions by approximately 90 s. This lag may be attributed to unavoidable error associated with warming of the components of the heated section. As such, a direct comparison of the experimental results and numerical predictions is impossible. However, the qualitative trends are in good agreement.

Comparison of the results of Fig. 2 and Figs. 6 and 7 is also made difficult because the dye of Fig. 2 behaves in a Lagrangian fashion, whereas the streamlines of Figs. 6 and 7 do not. However, it is evident that the dye must have originated at the heated surface since this is the only location characterized by upward velocities. In addition, the heated section is the origin of warm fluid parcels. If thermal diffusion is ignored, predicted isotherm contours will coincide with the outline of the dyed region of Fig. 2. Figures 2c ($t = 390$ s) and 6d ($t = 350$ s) show this qualitative agreement.

Numerical simulation of experiment 2 was curtailed at $t = 350$ s due to the expense of the computation.

Predicted vertical distributions of temperature, salinity, horizontal velocity and density above the heated section, at the edge of the heated section, and above the adiabatic section are shown for experiment 2 in Fig. 8. Thermal effects show temperature inversions which promote convection above the heated section (Fig. 8a). The warm temperatures are advected to locations above the adiabatic bottom section (Fig. 8c) at $t \simeq 350$ s. Warm temperatures were observed to reach $x = -50$ mm at $180\text{ s} < t < 360\text{ s}$ in the experiment as seen in Fig. 5a. The salinity near the bottom of the test cell becomes nearly uniform as evident in Fig. 8a. Salinities are redistributed by the convective motion at $x = -50$ and -100 mm and relatively high salinity, cool fluid resupplies the ascending, heated fluid (Fig. 8c). Conditions near the edge of the heated surface (Fig. 8b) show that thermally stratified conditions exist in the lower portions of the convective layer at later times, except for very near the bottom surface where lateral heat transfer from the heated surface provides a small effective bottom heat flux.

Density distributions are unstable above the heated section (Fig. 8d) due to the heating process. The salt-stratified fluid above the convecting layer (Fig. 8a) promotes a stable density distribution at this location (Fig. 8d). The density stratification is stable throughout the system above the adiabatic bottom section (Fig. 8f) and at the edge of the heated surface except for the fluid adjacent to the bottom of the test cell (Fig. 8c).

Horizontal velocity distributions illustrate the rotational motion of the large convection cells (Figs. 8e, f). However, a horizontal backflow is predicted to occur in the upper half of the secondary convecting layer at $x = -2$ mm.

The numerical predictions for experiment 4 are shown in Figs. 9 and 10. Although the trends for the onset and development of convection are similar to those of experiment 2, several differences are obvious. The time scale for experiment 4 is much smaller than experiment 2, while the roll cells, originating at the edge and above the heated strip, tend to extend to a greater height than those of experiment 2. This prediction is expected, due to the relatively large value of X, for experiment 4. The roll cells above the strip display a less organized structure in experiment 4 than was predicted for experiment 2.

As previously noted, convective motion originates, and is most energetic, near the edges of the heated strip (Figs. 9a and 10a). A second plume, however, develops near the symmetry plane and is much more energetic than the central plumes associated with

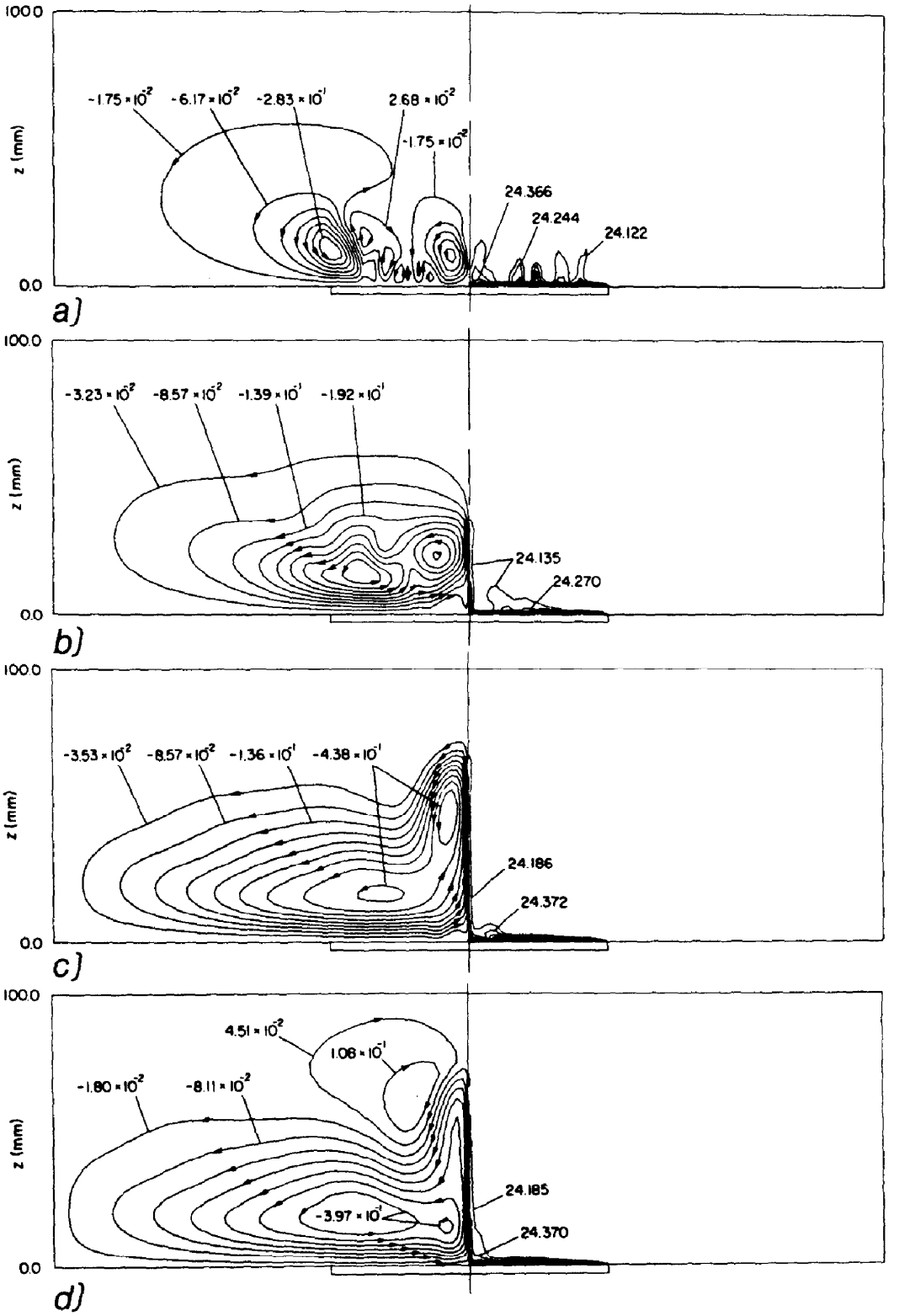

FIG. 9. Predicted streamlines (left) and isotherms (right) for experiment 4: (a) $t = 15$ s; (b) $t = 22.5$ s; (c) $t = 35$ s; (d) $t = 37.5$ s. Streamline and temperature values are s^{-1} and °C, respectively.

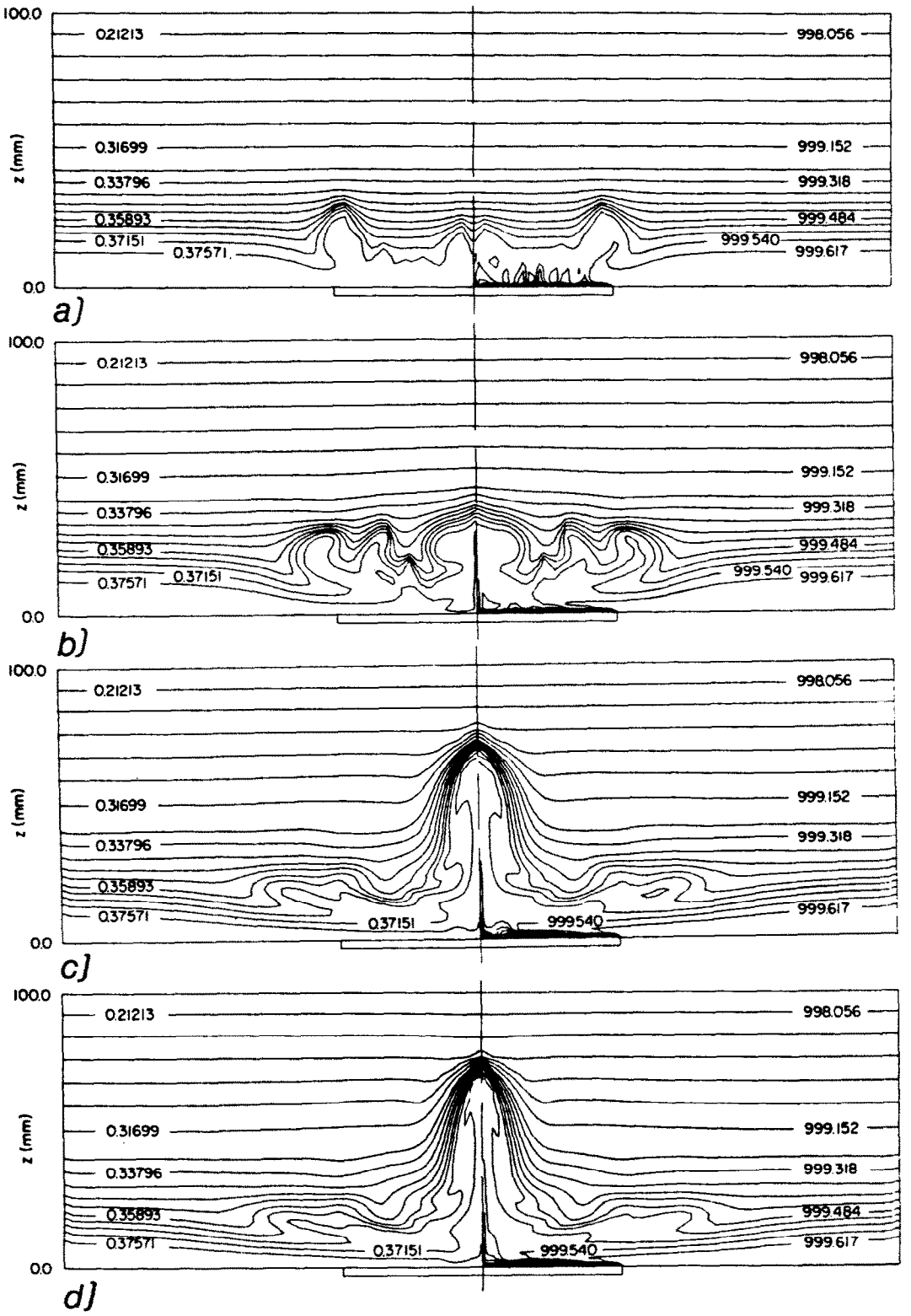

FIG. 10. Predicted salinity (left) and density (right) distributions for experiment 4: (a) $t = 15$ s; (b) $t = 22.5$ s; (c) $t = 35$ s; (d) $t = 37.5$ s. Salinity and density values are percent and kg m^{-3}, respectively.

experiment 2. As this plume begins to rise (Figs. 9b and 10b), the primary roll cells, which originated at the edges of the heater, immediately expand toward the symmetry plane to fill the void created by the departing central plume. Note that, as a rising plume loses it buoyancy (Fig. 9d), another plume develops just above the center of the heated strip. Figures 9c and 9d illustrate the oscillatory nature of plume formation at the symmetry plane, which is a consequence of the high X value associated with the simulation. The plumes are more energetic for this simulation than the simulation associated with experiment 2 and are capable of penetrating a considerable distance into the overlying stable fluid. Due to the high local curvature of the interface, old plumes tend to bounce downward as they lose their buoyant energy. This process in turn, delays the ascent of a new plume by causing a temporary pressure buildup at the heated surface, leading to the predicted oscillatory plume formation.

A final point worth noting is that there are two counter-rotating roll cells above the interface close to the symmetry plane (Fig. 9d) similar to the experimentally observed cells of Fig. 3d.

Comparison of the numerical predictions and experimental results reveals a significant time lag for experiment 4. Also, the extent of vertical plume propagation is predicted to be greater than observed in the experiments. This discrepancy may be attributed to the aforementioned error associated with warming of the test cell components or to possible three-dimensional effects. Indeed, flow visualization revealed a slightly three-dimensional plume structure in experiment 4. The two-dimensional model used in this study, which is not capable of simulating the dissipative effects of a third dimension, is, therefore, prone to overpredicting vertical plume propagation in experiments characterized by large X.

SUMMARY

An experimental and numerical investigation has been performed which considers a salt-stratified fluid layer destabilized by bottom heating from a discrete heat source.

Results of the investigation show that convective motion initially occurs near the edge of the heated strip where maximum horizontal density gradients are located. The edge roll cells propagate inward, consuming Rayleigh–Bénard-type convection cells located above the heated strip. Although this behavior may be expected, the study also reveals behavior which may not be anticipated.

Secondary layers are predicted to form above the bottom convective layer. A 'Christmas tree' type structure occurs above the bottom convective layer but could not be observed in the experiments due to small velocities associated with these roll cells or to the limited sensitivity of the flow visualization techniques. Rather than being driven by buoyancy considerations, the secondary layers rotate by way of shear stresses resulting from fluid motion in the main convection layer. These results may also provide clues for explaining the mechanisms by which mixed convective layers expand in salt-stratified fluid layers heated uniformly from below.

The study also reveals how the nature of secondary motion varies with the relative stability of the system. The size of the secondary convective cells decrease and their rotational speed increases as the destabilizing heat flux or stabilizing salt gradient are increased or decreased, respectively.

In general, qualitative agreement occurs between the experimental observations and the numerical predictions. Discrepancies between the experiment and the model may be traced to both unavoidable experimental error and limitations of the numerical model.

Acknowledgements—The work was performed at Purdue University. The authors would like to thank Professors F. P. Incropera and R. Viskanta for providing experimental facilities and expert counsel. Computational facilities were provided by Purdue University.

REFERENCES

1. M. E. Stern and J. S. Turner, Salt fingers and convecting layers, *Deep Sea Res.* **16,** 497–511 (1969).
2. L. H. Kantha, A note on the effect of viscosity on double-diffusive processes, *J. geophys. Res.* **85,** 4398–4404 (1980).
3. H. Tabor, Solar Ponds, *Sol. Energy* **27,** 181–194 (1981).
4. C. F. Chen and J. S. Turner, Crystallization in a double-diffusive system, *J. geophys. Res.* **85,** 2573–2593 (1980).
5. H. E. Huppert and P. F. Linden, On heating a stable salinity gradient from below, *J. Fluid Mech.* **95,** 431–464 (1979).
6. C. J. Poplawsky, F. P. Incropera and R. Viskanta, Mixed layer development in a double-diffusive, thermohaline system, *Trans. Am. Soc. mech. Engrs*, Series J, *J. Sol. Energy Engng* **103,** 351–359 (1981).
7. W. T. Lewis, F. P. Incropera and R. Viskanta, Interferometric study of mixed layer development in a laboratory simulation of solar pond conditions, *Sol. Energy* **28,** 389–401 (1982).
8. W. T. Lewis, F. P. Incropera and R. Viskanta, Interferometric study of stable salinity gradients heated from below or cooled from above, *J. Fluid Mech.* **116,** 411–430 (1982).
9. D. T. J. Hurle and E. Jakeman, Introduction to the technique of crystal growth, *Physico-Chem. Hydrodynam.* **2,** 237–244 (1981).
10. S. Ostrach, Fluid mechanics of crystal growth—the 1982 Freeman Scholar Lecture, *Trans. Am. Soc. mech. Engrs*, Series I, *J. Fluids Engng* **105,** 5–20 (1983).
11. T. A. Newell and J. R. Hull, Depth sounding diagnostic measurement of salt gradient solar ponds, *Trans. Am. Soc. mech. Engrs*, Series J, *J. Sol. Energy Engng* **107,** 160–164 (1985).
12. F. P. Incropera, C. E. Lents and R. Viskanta, Gradient layer entrainment in a double-diffusive thermohaline system with mixed layer circulation, *Trans. Am. Soc. Mech. Engrs*, Series J, *J. Sol. Energy Engng* (in press).
13. R. H. Hubbell and B. Gebhart, Transport processes induced by a heated cylinder submerged in a salt stratified medium, *Proc. 24th Heat Transfer and Fluid Mechanics Institute*, Corvallis, OR, U.S.A. (June 1974).
14. Y. D. Chashehkin and V. A. Popov, The structure of free convective flow above a heated cylinder in a stratified fluid, *Sov. Phys. Dokl.* **24,** 827–828 (1980).

15. A. B. Tsinobar, Y. Yahalom and D. J. Shlien, A point source of heat in a stable salinity gradient, *J. Fluid Mech.* **135,** 199–217 (1983).
16. Sylox 2, micron-sized silica, manufactured by Davison Chemical Co., Baltimore, MD 21203, U.S.A.
17. T. L. Bergman, F. P. Incropera and R. Viskanta, A differential model for salt-stratified, double-diffusive systems heated from below, *Int. J. Heat Mass Transfer* **28,** 779–788 (1985).
18. J. S. Turner, *Buoyancy Effects in Fluids*. Cambridge University Press, Cambridge (1979).
19. United States Office of Saline Water, Technical Data Book (1964).
20. S. V. Patankar, *Numerical Heat Transfer and Fluid Flow*. McGraw-Hill, New York (1980).
21. S. V. Patankar, A calculation procedure for two-dimensional elliptical situations, *Numer. Heat Transfer* **4,** 409–425 (1981).
22. T. L. Bergman, F. P. Incropera and R. Viskanta, Parameterization of system behavior for salt-stratified solutions heated from below with and without salinity-maintained mixed layers, *Int. J. Heat Mass Transfer* **28,** 1617–1621 (1985).
23. C. F. Chen, D. G. Briggs and R. A. Wirtz, Stability of thermal convection in a salinity gradient due to lateral heating, *Int. J. Heat Mass Transfer* **14,** 57–65 (1971).
24. H. E. Huppert, R. C. Kerr and M. A. Hallworth, Heating or cooling a stable compositional gradient from the side, *Int. J. Heat Mass Transfer* **27,** 1395–1401 (1984).
25. K. E. Torrance, Natural convection in thermally stratified enclosures with localized heating from below, *J. Fluid Mech.* **95,** 477–495 (1979).
26. N. C. Markatos and M. R. Malin, Mathematical modelling of buoyancy-induced smoke flow in enclosures, *Int. J. Heat Mass Transfer* **25,** 63–75 (1982).

ETUDE EXPERIMENTALE ET NUMERIQUE D'UNE CONVECTION A DIFFUSION DOUBLE INDUITE PAR UNE SOURCE DISCRETE DE CHALEUR

Résumé—Des systèmes industriels variés tels que les techniques de croissance des cristaux ou les bassins solaires, peuvent être caractérisés par un comportement de double diffusion induit par des sources discrètes de chaleur. L'objet de cette étude est de préciser la convection induite par le chauffage inférieur avec un ruban chaud, limité, placé sous une couche de fluide stratifiée en sel. On porte l'attention sur la formation et la croissance des régions convectives dans le fluide stratifié. Les résultats expérimentaux et numériques montrent que le développement des conditions convectives est caractérisé par une interaction entre la convection de type Rayleigh–Bénard et les rouleaux longitudinaux convectifs formés par des gradients de température horizontaux. L'écoulement secondaire est visualisé au-dessus de la cellule inférieure de convection. Pour des combinaisons relativement instables de stratification et de flux thermique appliqué, on observe une interaction compliquée entre une convection chaotique à diffusion double et une distribution tridimensionnelle à onde de gravité.

EXPERIMENTELLE UND NUMERISCHE UNTERSUCHUNG DER DURCH EINE DISKRETE WÄRMEQUELLE HERVORGERUFENEN DOPPEL-DIFFUSIVEN KONVEKTION

Zusammenfassung—Verschiedene technische Systeme, die zum Beispiel mit Kristallwachstum oder mit Solarponds zu tun haben, können durch ein doppel-diffusives Verhalten—hervorgerufen durch diskrete Wärmequellen—charakterisiert werden. Das Ziel dieser Arbeit ist, die Doppeldiffusion zu untersuchen, die durch Beheizung von unten mittels eines endlichen beheizten Streifens hervorgerufen wird, welcher unterhalb einer salz-geschichteten Fluidschicht liegt. Der Formation und dem Wachsen der Konvektionsgebiete in dem salz-geschichteten Fluid wird besondere Aufmerksamkeit gewidmet. Die experimentellen und numerischen Ergebnisse zeigen, daß die Entwicklung von Konvektionsbedingungen durch ein Zusammenwirken von Rayleigh–Benárd Konvektion und konvektiven Längs–Walzen beschrieben wird, welche auf Grund horizontaler Temperaturgradienten entstehen. Die Sekundärströmung wird sichtbar gemacht. Sie tritt über der Konvektionszelle am Grund auf. Für relativ instabile Kombinationen der Salzschichtung und der aufgeprägten Wärmestromdichte wird ein kompliziertes Zusammenspiel aus chaotischer doppeldiffusiver Konvektion und dreidimensionaler Dichtewellenverteilung beobachtet.

ЭКСПЕРИМЕНТАЛЬНОЕ И ЧИСЛЕННОЕ ИССЛЕДОВАНИЕ ДВУХДИФФУЗИОННОЙ КОНВЕКЦИИ, ВЫЗВАННОЙ ДИСКРЕТНЫМ ИСТОЧНИКОМ ТЕПЛА

Аннотация—Различные инженерные устройства, как, например, системы, связанные с выращиванием кристаллов или с солнечными бассейнами, могут характеризоваться двухдиффузионной конвекцией, вызванной дискретными источниками тепла. Цель работы—изучение двухдиффузионной конвекции, инициированной нагревом снизу в полосе конечной длины, расположенной под слоем жидкости, стратифицированной распределением концентрации в ней соли. Особое внимание уделено образованию и распространению конвективных областей в жидкости с солевой стратификацией. Экспериментальные и численные результаты показывают, что развитие конвективных режимов характеризуется взаимодействием между конвекцией типа Рэлея–Бенара и продольными конвективными валами, индуцированными горизонтальными температурными градиентами. Визуализировано в эксперименте и предсказано в расчетах появление вторичного течения в нижней части конвективной ячейки. Для относительно неустойчивых состояний солевой стратификации и прилагаемого теплового потока обнаружено сложное взаимодействие между хаотичной, двухдиффузионной конвекцией и трехмерным распределением валов гравитационных волн.